Draft version March 15, 2013
Preprint typeset using LaTeX style emulateapj v. 5/2/11

arXiv:1303.3270v1 [astro-ph.HE] 13 Mar 2013

MASS AND RADIUS CONSTRAINTS USING MAGNETAR GIANT FLARE OSCILLATIONS

Alex T. Deibel [1], Andrew W. Steiner [2], and Edward F. Brown [1,3]

Draft version March 15, 2013

ABSTRACT

We study crustal oscillations in magnetars including corrections for a finite Alfvén velocity. Our crust model uses a new nuclear mass formula that predicts nuclear masses with an accuracy very close to that of the Finite Range Droplet Model. This mass model for equilibrium nuclei also includes recent developments in the nuclear physics, in particular, shell corrections and an updated neutron-drip line. We perturb our crust model to predict axial crust modes and assign them to observed giant flare quasi-periodic oscillation (QPO) frequencies from SGR 1806-20. The QPOs associated with the fundamental and first harmonic can be used to constrain magnetar masses and radii. We use these modes and the phenomenological equations of state from Steiner et al. to find a magnetar crust which reproduces observations of SGR 1806-20. We find magnetar crusts that match observations for various magnetic field strengths, entrainment of the free neutron gas in the inner crust, and crust-core transition densities. Matching observations with a field-free model we obtain the approximate values of $M = 1.35\ \mathrm{M}_{\odot}$ and $R = 11.9$ km. Matching observations using a model with the surface dipole field of SGR 1806-20 ($B = 2.4 \times 10^{15}$ G) we obtain the approximate values of $M = 1.25\ \mathrm{M}_{\odot}$ and $R = 12.4$ km. Without significant entrainment of the free neutron gas the magnetar requires a larger mass and radius to reproduce observations. If the crust-core transition occurs at a lower density the magnetar requires a lower mass and a larger radius to reproduce observations.

Subject headings: dense matter — stars: neutron — stars: magnetic fields — stars: oscillations

1. INTRODUCTION

Highly magnetized and isolated neutron stars, known as magnetars, emit irregular and extremely energetic gamma ray flares. These flares are thought to occur following a starquake, in which the magnetar's crust is fractured by a reconfiguring magnetic field. Quasi-periodic oscillations (QPOs) are observed in the tails of giant flare emissions (Barat et al. 1983; Israel et al. 2005; Strohmayer & Watts 2005; Watts & Strohmayer 2006). Torsional modes of the oscillating crust successfully explain most QPOs (Duncan 1998; Piro 2005; Strohmayer & Watts 2006; Samuelsson & Andersson 2007). Another model associates QPOs with magneto-hydrodynamic (MHD) modes in the core (Glampedakis et al. 2006; Levin 2006). Neither model is able to predict all of the observed mode frequencies. Crustal oscillations cannot easily reproduce all of the low-frequency modes, and core MHD modes are unable to reproduce the highest QPO frequencies observed (van Hoven & Levin 2012).

Resolving these two models and obtaining a complete understanding of the mode structure in a highly magnetized neutron star remains challenging. Nevertheless, if some of the observed QPOs are associated with the torsional modes of the neutron star crust, then magnetars can give a unique insight into the microphysics of the neutron star crust, e.g., the nuclear symmetry energy (Steiner & Watts 2009). In this work, we assume that one of the lower QPO frequencies and the 626 Hz mode observed from SGR 1806-20 both represent the torsional modes of the crust. If this is indeed the case, constraints on the mass and radius of the magnetar can be obtained (Samuelsson & Andersson 2007; Lattimer & Prakash 2007).

This study uses modern equations of state (EOSs) to predict torsional mode frequencies and compares them to observed QPO frequencies to determine magnetar masses and radii. The crust EOS is based on a liquid droplet model which predicts nuclear masses to within 1.2 MeV (Steiner 2012), close to the accuracy obtained in the Finite Range Droplet Model (Möller et al. 1995). The core EOS is based on recent neutron star mass and radius constraints from observations of photosphere radius expansion bursts (PREs) and the quiescent emission of low-mass X-ray binaries (LMXBs) (Steiner et al. 2010; Steiner et al. 2012). At each baryon density we compute the shear modulus based on the equilibrium configuration of nuclei. This study also examines the effects of a magnetic field in an oscillating neutron star crust model. By adding the effect of the magnetic field on electrons, as in Broderick et al. (2000), we revise the magnetic composition of the crust (Lai & Shapiro 1991) with a new determination of equilibrium nuclei. To describe the oscillating crust we use the axial perturbation equations with general relativistic corrections (Schumaker & Thorne 1983; Samuelsson & Andersson 2007) and include the magnetic field as done for the non-relativistic case (Piro 2005; Steiner & Watts 2009).

In §2 we present the magnetized crust composition based on our mass model (a detailed description of this formalism is in Appendix A). Section 3 contains a summary of the axial perturbation equations for the crust modes. We then use, in §4, the predicted fundamental and harmonic frequencies, along with the magnetized crust composition, to constrain the masses and radii of

---

[1] Department of Physics and Astronomy, Michigan State University, East Lansing, MI 48824 deibelal@msu.edu
[2] Institute for Nuclear Theory, University of Washington, Seattle, WA 98195
[3] National Superconducting Cyclotron Laboratory, East Lansing, MI 48824

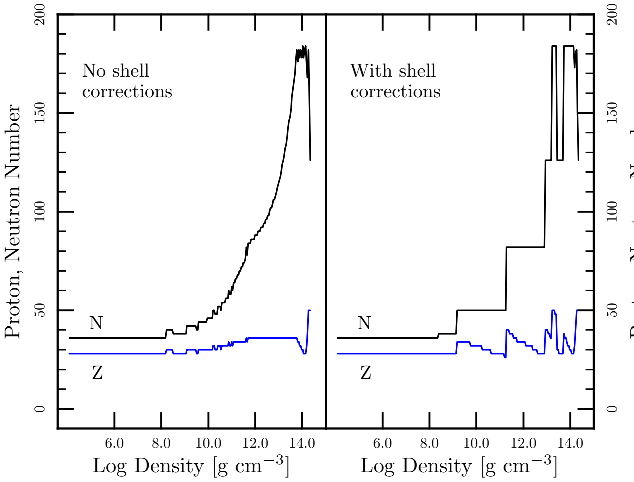

Fig. 1.— Equilibrium composition of the crust without a magnetic field for a model that neglects shell effects (left panel) and for a model that includes them (right panel). The blue lower curve corresponds to the proton number (Z) and the black upper curve corresponds to the neutron number (N).

magnetars.

2. CRUST COMPOSITION

For an isolated neutron star we determine the crust composition by finding the equilibrium nucleus at a given baryon density. At the temperatures of interest, typically $T < 10^9$ K, the crust consists of only one nucleus at a given depth. The outer crust consists of a lattice of nuclei embedded in a degenerate electron Fermi gas (Baym et al. 1971a). The neutron-drip point, the point at which it becomes energetically favorable for neutrons to drip out of nuclei, defines the boundary between the outer and inner crust. The inner crust can then be described as a lattice of nuclei embedded in both an electron and neutron gas (Baym et al. 1971a). As described in Appendix A, at a given proton number Z, atomic number A, and baryon density n, the total energy density of the crust will have contributions from the nuclear binding energy, the Coulomb lattice, the electron gas, and the neutron gas. At a given baryon density the equilibrium nucleus minimizes the total energy density of the system. The most energetically favorable nuclei tend to contain a closed shell of protons or neutrons due to shell corrections. As density increases equilibrium nuclei will move to higher closed shells of protons and neutrons with the most neutron-rich nuclei seen between the neutron-drip point and the crust-core transition. The above features of the crust composition can be seen in Figure 1. We ignore the deformation of nuclei at high densities in the crust composition.

In the outer crust a strong magnetic field will force electrons to occupy the lowest Landau levels. At higher baryon densities electrons can occupy higher Landau levels and thus their energy density approaches the field-free case. For this reason, as seen in Table 1, only the outer crust equilibrium composition is significantly altered. For $B < 10^{18}$ G we can ignore both the effect of the magnetic field on the structure of the nuclei in the crust (see, e.g., Harding & Lai 2006; Nag et al. 2009) and on the gross structure of the neutron star (Cardall et al. 2001). Qualitatively similar results have also been obtained in Chamel et al. (2012) using Hartree-Fock-Bogoliubov instead of our liquid droplet model.

3. TORSIONAL OSCILLATIONS IN A STRONG MAGNETIC FIELD

We describe the axial crust modes of an oscillating neutron star following the work of Schumaker & Thorne (1983) and Samuelsson & Andersson (2007). We combine two forms of the axial perturbation equation. In the non-magnetic case, the equation for the axial perturbation ξ can be written in the form (Samuelsson & Andersson 2007) $\xi'' + F'\xi' + G\xi = 0$, in which primes indicate derivatives with respect to the radial coordinate, and F and G are functions of the shear velocity v_s and the metric functions ν and λ for a static and spherically symmetric spacetime metric, $\mathrm{d}s^2 = -e^{2\nu}\mathrm{d}t^2 + e^{2\lambda}\mathrm{d}r^2 + r^2\left(\mathrm{d}\theta^2 + \sin^2\theta\,\mathrm{d}\phi^2\right)$. The radial component of the perturbation is suppressed due to the strong vertical stratification. Working in the isotropic limit, we incorporate corrections for a finite Alfvén velocity $v_\mathrm{A} = B/\sqrt{4\pi\rho_i}$ by analogy with the Newtonian expressions (Piro 2005; Steiner & Watts 2009). The result is

$$(v_s^2 + v_\mathrm{A}^2)\xi'' + v_s^2 \frac{\mathrm{d}}{\mathrm{d}r}\left\{\ln\left[r^4 e^{\nu-\lambda}\left(\varepsilon + p\right) v_s^2\right]\right\}\xi' + e^{2\lambda}\left[e^{-2\nu}\omega^2\left(1 + \frac{v_\mathrm{A}^2}{c^2}\right) - \frac{\left(l^2 + l - 2\right) v_s^2}{r^2}\right]\xi = 0. \quad (1)$$

In this expression r is the radius, ε is the energy density, p is the pressure, ω is the angular frequency, and l is the angular wavenumber. The shear velocity is $v_s = \sqrt{\mu/\rho}$. Here μ is the shear modulus, for which we use the formulation appropriate for a body-centered cubic lattice (Strohmayer et al. 1991),

$$\mu = \frac{0.1194\Gamma}{1 + 0.595(\Gamma_0/\Gamma)^2} n_i k_\mathrm{B} T. \quad (2)$$

We integrate equation (1) over the solid crust, which lies between the crust-core interface at $r = R_\mathrm{core}$ and where the lattice melts at $r = R_\mathrm{crust}$. The melting transition is determined by where the plasma coupling parameter $\Gamma = (Ze)^2/ak_\mathrm{B}T = \Gamma_\mathrm{melt} = 175$ (Farouki & Hamaguchi 1993; Horowitz et al. 2010). Here $a = (3/4\pi n_i)^{1/3}$ is the radius of the Wigner-Seitz cell, Z is the atomic charge number, n_i is the ion number density, and the temperature is T $= 3.0 \times 10^8$ K.

For the boundary conditions needed to solve equation (1), we require the traction, ξ', to vanish at the top and bottom of the crust. This is a good approximation near the surface where pressure vanishes. The description of matter near the crust-core transition is complicated by the appearance of nuclear pasta. Since the quasi-free neutrons are superfluid, assuming the traction vanishes at the crust-core boundary may also be a good approximation. An additional impact of the superfluid is that some fraction, f_ent, of the quasi-free neutrons are entrained with the nuclei (Chamel et al. 2012; Chamel 2013). We assume zero traction at the crust-core transition and leave a more complete description of matter at the highest densities to future work.

For a given l, equation (1), when integrated over the crust with the boundary conditions described here, has an eigenvalue ω that is uniquely determined by the crust

TABLE 1
MAGNETIC EQUILIBRIUM NUCLEI BELOW CRUST-CORE TRANSITION

	$\rho_{\max}$ (g cm^{-3})				
Nuclei	$B_* = 0$	$B_* = 1$	$B_* = 10$	$B_* = 10^2$	$B_* = 10^3$
$^{50}_{22}$Ti	3.96×10^8		4.15×10^8	1.80×10^9	9.90×10^9
$^{66}_{28}$Ni	1.10×10^9		1.16×10^9	2.79×10^9	1.96×10^{10}
$^{48}_{20}$Ca	1.41×10^9			–	–
$^{84}_{34}$Se	5.52×10^9			4.76×10^9	5.20×10^{10}
$^{82}_{32}$Ge	1.69×10^{10}			1.61×10^{10}	7.32×10^{10}
$^{80}_{30}$Zn	3.88×10^{10}				9.81×10^0
$^{78}_{28}$Ni	1.52×10^{11}				1.60×10^{11}
$^{76}_{26}$Fe	1.85×10^{11}				1.68×10^{11}
$^{122}_{40}$Zr	2.48×10^{11}				1.94×10^{11}
$^{120}_{38}$Sr	3.49×10^{11}				3.85×10^{11}
$^{118}_{36}$Kr	5.15×10^{11}				5.68×10^{11}
$^{116}_{34}$Se	1.18×10^{12}				
$^{114}_{32}$Ge	2.34×10^{12}				
$^{112}_{30}$Zn	3.81×10^{12}				
$^{110}_{28}$Ni	8.32×10^{12}				
$^{166}_{40}$Zr	1.06×10^{13}				

NOTE. — We adopt the format of Lai & Shapiro (1991) where $\rho_{\max}$ is the maximum mass density where the equilibrium nucleus is present. If a density value is unchanged the following column is blank. Here $B_* = B/(4.414 \times 10^{13}\,\mathrm{G})$, which is the ratio of the magnetic field to the critical field, defined as the field at which the cyclotron energy equals the electron rest-mass.

thickness $\Delta = R_{\rm crust} - R_{\rm core}$ and the neutron star radius. These in turn depend on the equation of state.

4. MAGNETAR MASSES AND RADII

For the core, we use the probability distribution for the EOS determined by Steiner et al. (2012) from observations of PREs and from the quiescent emission of LMXBs. In this work, we use a range of five high-density EOSs corresponding to the most probable equation of state along with its 1 and 2-σ lower and upper bounds.

QPO frequencies have been detected in two magnetars, SGR 1806−20 and SGR 1900+14 (Israel et al. 2005; Strohmayer & Watts 2005; Watts & Strohmayer 2006; Strohmayer & Watts 2006). The 29 Hz mode in SGR 1806−20 and the 28 Hz mode in SGR 1900+14 are often assumed to be the fundamental torsional modes, but an 18 Hz mode was also observed in SGR 1806−20 and a lower frequency mode is not ruled out by the 1900+14 data. SGR 1806−20 also showed a very clear 626 Hz mode, possibly matching the first radial harmonic ($n = 1$). Several other modes are observed between 50 and 200 Hz, and these can be matched with higher angular momentum harmonics, $l > 0$.

Each equation of state gives mass-radius combinations with different crust thicknesses, and hence a unique fundamental mode ($n = 0$) and harmonic mode ($n = 1$). We can constrain the masses and radii of magnetars by matching predicted fundamental modes and harmonic modes to observed QPOs. While GR tends to decrease the frequencies, softer core equations of state with smaller radii tend to increase the frequencies. Because of this latter effect, we get frequencies which are larger than that obtained in Steiner & Watts (2009). The $n = 0$, $l = 2$ mode corresponds to the 29 Hz QPO of SGR 1806-20. Our model predicts $n = 1$ harmonic modes near 600 Hz and we compare these predicted modes with the 626 Hz QPO of SGR 1806-20.

To find crusts with fundamentals that match the 29 Hz QPO we model crust perturbations in magnetars between 0.8–2.0 $\mathrm{M}_\odot$ with magnetic fields matching the surface dipole field of SGR 1806-20. Whichever crust has an $n = 0$, $l = 2$ mode that matches the 29 Hz QPO we take as the crust of the magnetar. This method is demonstrated in Figure 2 where crusts are constructed using the SLy4 crust EOS (Chabanat et al. 1995). Crusts with harmonics that match the 626 Hz QPO are found using an identical technique. Whichever crust has a $n = 1$ mode which reproduces the observed QPO we take as crust of the magnetar. The same analysis is repeated for the 1 and 2-σ lower and upper bounds on the core EOS.

A comparison of masses and radii from fundamental and harmonic modes can be seen in Figure 3. The intersection of fundamental and harmonic masses and radii on the mass versus radius plot gives a crust that best matches the properties of SGR 1806-20. The mass and radius found for SGR 1806-20 depend on the properties of the interior of the magnetar which determine the fundamental and harmonic modes. This study focuses on varying three aspects of the interior physics that remain unknown, namely, the magnetic field strength in the crust, the crust-core transition density, and the degree of free neutron entrainment in the inner crust.

First, we examine the sensitivity of fundamental and harmonic modes to the strength of the magnetic field. Strong magnetic fields melt the outermost boundary of the crust (i.e., push the melting point of the one-component plasma to higher pressures). Since $R_{\rm core}$ remains fixed and $R_{\rm crust}$ decreases, a strong magnetic field thins the crust (i.e., decreases Δ). Although a strong magnetic field can decrease the crust thickness and change the composition of the outer crust, the overall impact on predicted fundamental and harmonic mode frequencies is negligible. We find that predicted fundamental modes from magnetized crusts are nearly identical to the field-free case. The magnetic field is not

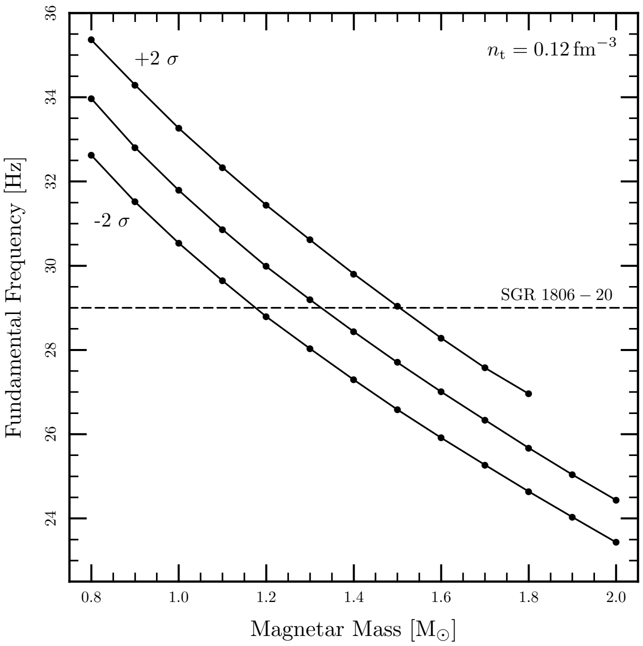

FIG. 2.— Frequency of the fundamental $l = 2$ mode as a function of the magnetar mass for the core EOS probability distribution (centroid and $\pm 2\sigma$) from Steiner et al. (2012) and an SLy4 crust EOS. The dashed black line indicates the observed 29 Hz QPO of SGR 1806-20. The frequencies are evaluated for a crust-core transition density of $0.12\,\mathrm{fm}^{-3}$ with $B = 0$ G.

a determining factor because fundamental crust modes are entirely set by our choice of radius for the magnetar. That is, fundamental modes are entirely set by the equation of state. However, a magnetized crust can significantly alter predicted harmonic modes. The $n = 1$ modes are sensitive to the magnetic field, especially in the outer crust where $v_A > v_s$ (Piro 2005; Nandi et al. 2012). The magnetized crusts that match observed QPOs can be seen in Figure 3.

We test two extreme values for the crust-core transition density, n_t, from Oyamatsu & Iida (2007). The exact value of the crust-core transition density is unknown, in part because the density dependence of the nuclear symmetry energy in the inner crust is not well constrained and also because of the possible existence of nuclear pasta (see e.g. Newton et al. 2013). In Figure 3, for each transition density we examine various magnetic field strengths to find masses and radii from intersections of fundamentals and harmonics. For a larger crust-core transition at $0.12\,\mathrm{fm}^{-3}$ and at the surface dipole field of SGR 1806-20[4] ($B = 2.4 \times 10^{15}$ G) we find the magnetar to have $M = 1.25\,\mathrm{M}_\odot$ and $R = 12.4\,\mathrm{km}$. We must extrapolate outside the equation of state curves to approximate a mass and radius for the lower crust-core transition density $0.08\,\mathrm{fm}^{-3}$. This crust-core transition gives $M = 0.96\,\mathrm{M}_\odot$ and $R = 13.5\,\mathrm{km}$ for SGR 1806-20. In either case, if we assume that the magnetic field inside the crust is larger than the observed surface field, then a smaller mass and larger radius is implied. If the magnetic field is too large, the implied radius will be far outside radii implied by mass and radius observations from the quiescent LMXBs in M13 and ω Cen (Steiner et al. 2010).

As can be seen in Figure 3, only harmonic modes are affected by a change in the crust-core transition density. A change in the crust-core transition density will change the crust thickness and harmonic modes scale with the crust thickness. Fundamental modes remain unchanged, however, because they scale with the radius of the entire star.

Entrainment of the free neutron gas in the inner crust alters both fundamental and harmonic modes. We determine the degree of entrainment by the fraction of the free neutron gas that moves with the nuclei lattice during a crust oscillation. The intermediate cases of $f_\mathrm{ent} = 0.75$ and 0.50 can be seen in Figure 4. If a lower fraction of the free neutrons are entrained, then larger masses and radii are implied for the magnetar. It can be seen in Figure 4 that fundamental modes are significantly altered by the degree of entrainment. This occurs because the fundamental mode energy is concentrated deeper in the crust, whereas harmonic modes have their energy distributed more uniformly over the crust (Piro 2005). We find that a large degree of entrainment, $f_\mathrm{ent} > 0.75$, is required for predicted crust modes to match observed QPOs using crust models built upon the SLy4 interaction (Chabanat et al. 1995). In contrast, for the Rs model (Friedrich & Reinhard 1986) a low degree of entrainment is required, $f_\mathrm{ent} = 0.20 - 0.30$.

For comparison, we repeat the above analysis with the Rs crust equation of state (Friedrich & Reinhard 1986). This EOS gives frequencies between 15–20 Hz for the $n = 0$, $l = 2$ fundamental mode. Therefore, we must assign the predicted fundamental modes from Rs to the observed 18 Hz QPO. The density derivative of the nuclear symmetry energy, L, is different in the Rs model and the SLy4 model. The Rs model corresponds to $L = 86$ MeV whereas the SLy4 model has $L = 46$ MeV. The Rs model has a smaller fundamental frequency than SLy4 because it has a larger L value.

The Rs EOS also gives harmonic modes consistent with the 626 Hz QPO. Using the Rs EOS and a larger crust-core transition at $0.12\,\mathrm{fm}^{-3}$ and at the surface dipole field of SGR 1806-20 ($B = 2.4 \times 10^{15}$ G) we find the magnetar to have $M = 1.10\,\mathrm{M}_\odot$ and $R = 13.8\,\mathrm{km}$. In Figure 5 we show the fundamental and harmonic mode intersections for various magnetic fields. Finally, we examine the effect of entrainment on frequencies predicted by the Rs EOS. The predicted $n = 0$, $l = 2$ fundamental gives frequencies near the 29 Hz QPO of SGR 1806-20 when there is a low degree of entrainment of the free neutrons. The behavior of the fundamental with the degree of entrainment can be seen in Figure 6. For example, for $\mathrm{f}_\mathrm{ent} = 0.25$ we find the magnetar to have $M = 1.12\,\mathrm{M}_\odot$ and $R = 12.0\,\mathrm{km}$.

5. DISCUSSION

Fundamental and harmonic modes are altered by the presence of a magnetic field, by the degree of entrainment of the free neutron gas in the inner crust, and by the location of the crust-core transition. Although the observed surface dipole field strengths are too weak to affect the fundamental torsional modes of magnetars, the harmonic modes are significantly altered by fields $\gtrsim 10^{15}$ G. For a higher transition density at $0.12\,\mathrm{fm}^{-3}$ a magnetic field of $B \gtrsim 4.0 \times 10^{15}$ G gives no mass and radius solutions consistent with the mass and radius constraints from PREs and LMXBs. For larger magnetic fields extrapolation

---

[4] McGill SGR/AXP Online Catalog, `http://www.physics.mcgill.ca/~pulsar/magnetar/main.html`

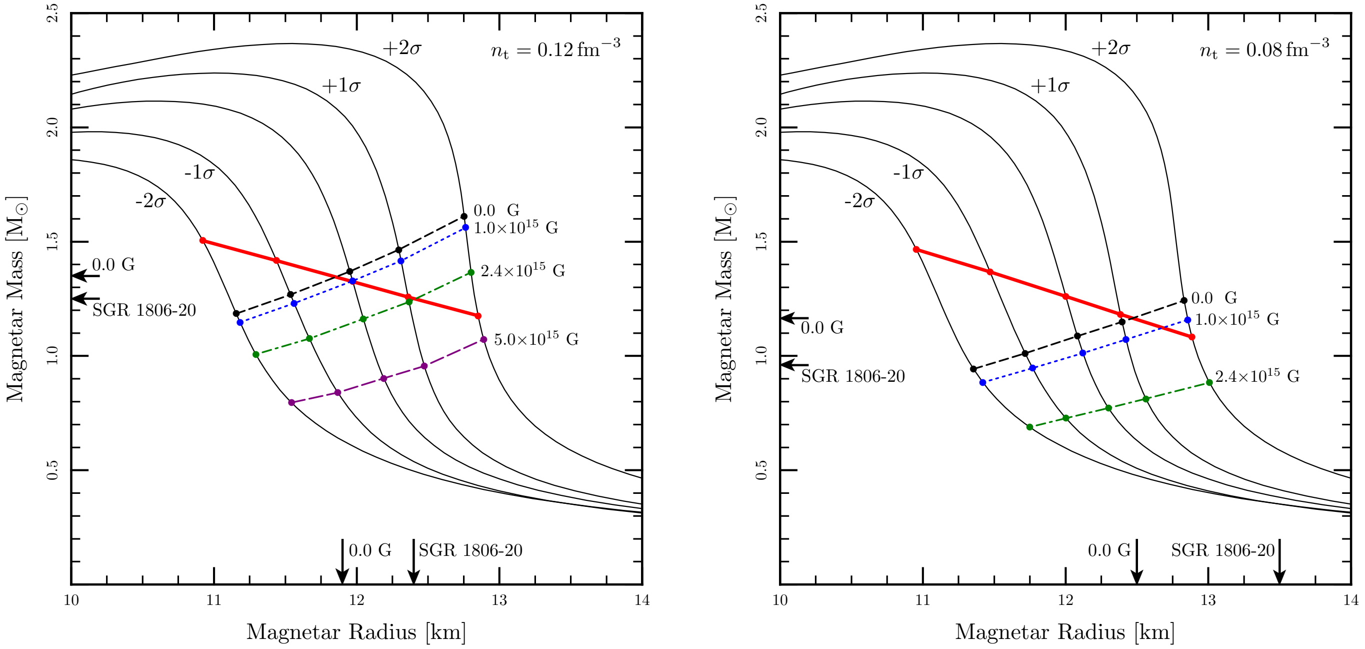

FIG. 3.— Magnetar mass as a function of radius for the core EOS probability distribution from Steiner et al. (2012). Frequencies are evaluated using the SLy4 crust EOS for two different crust-core transition densities, $n_t = 0.12\,\mathrm{fm}^{-3}$ (left plot) and $n_t = 0.08\ \mathrm{fm}^{-3}$ (right plot). The thick red solid line indicates masses and radii for which the fundamental mode has a frequency of 29 Hz. The black short-dashed line indicates masses and radii for a 626 Hz harmonic mode and $B = 0$ G. Masses and radii from 626 Hz harmonic modes with magnetized crusts are labeled accordingly. Arrows indicate masses and radii that match both the fundamental and the harmonic modes for the field-free case and the case with the magnetic field of SGR 1806-20 ($B = 2.4 \times 10^{15}$ G).

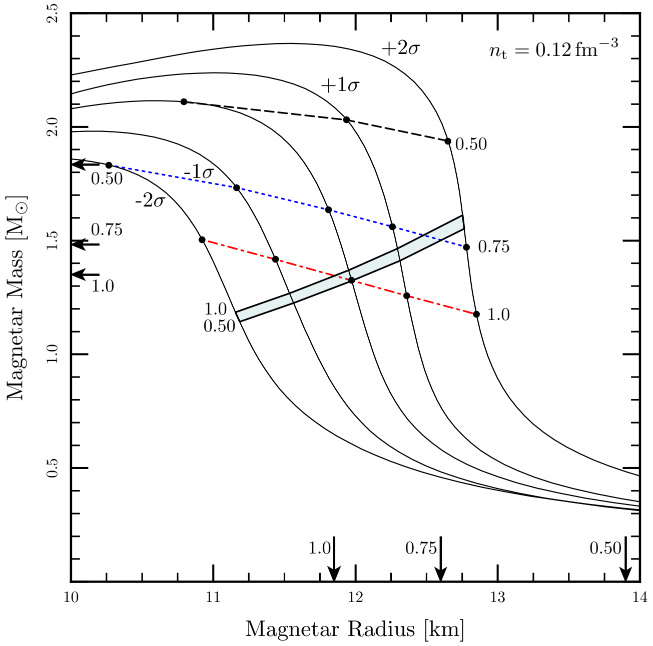

FIG. 4.— Magnetar mass as a function of radius for EOS probability distribution from Steiner et al. (2012). Frequencies are evaluated using the SLy4 crust EOS with $B = 0$ G and $n_t = 0.12\ \mathrm{fm}^{-3}$. The red dot-dashed, blue dotted, and black dashed lines indicate masses and radii from fundamental modes of frequency 29 Hz for different free neutron entrainment fractions f_{ent}. The shaded band indicates masses and radii from 626 Hz harmonic modes as f_{end} is varied from 0.50 to 1.0. Arrows indicate the masses and radii that match both the fundamental and the harmonic modes for $f_{\mathrm{ent}} = 1.0$, 0.75, and 0.50.

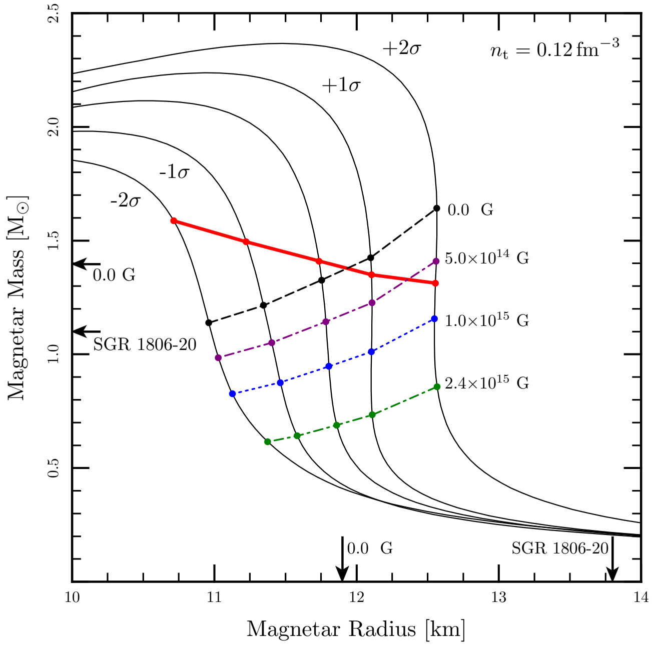

FIG. 5.— The same as Fig. 3, but for the Rs crust EOS with $n_t = 0.12\ \mathrm{fm}^{-3}$ and for a 18 Hz fundamental frequency. The thick red solid line indicates masses and radii determined from fundamental modes. Masses and radii from harmonic modes with magnetized crusts are labeled accordingly. Arrows indicate masses and radii that match both the fundamental and the harmonic modes for the field-free case and the case with the magnetic field of SGR 1806-20 ($B = 2.4 \times 10^{15}$ G).

outside of the EOS curves is necessary or another EOS is needed. The same is true for a lower crust-core transition at $0.08\,\mathrm{fm}^{-3}$ and a magnetic field of $B \gtrsim 2.0 \times 10^{15}$ G.

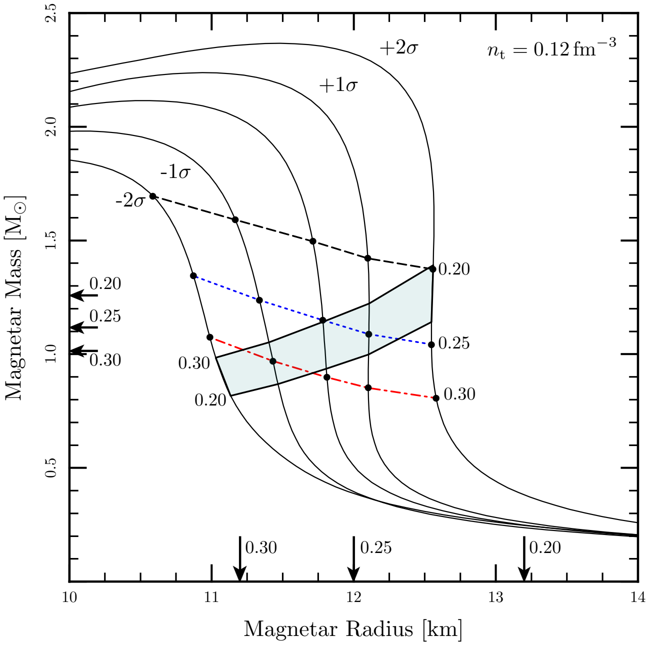

Fig. 6.— The same as Fig. 4, but for the Rs crust EOS with $B = 0\,{\rm G}$. Here the free neutron entrainment fraction $f_{\rm ent}$ is varied from 0.20 to 0.30, with $f_{\rm ent}$ labeled next to the corresponding curves. The red dot-dashed, blue dotted, and black dashed lines indicate masses and radii from the 29 Hz fundamental mode. The shaded band indicates masses and radii from the 626 Hz harmonic mode. Arrows indicate the masses and radii for $f_{\rm ent} = 0.30$, 0.25, and 0.20 that match both the fundamental and harmonic modes.

For both transition densities we find crusts for the field-free case and for various magnetic fields as seen in Figure 3. For all transition densities a magnetized crust requires a lower mass than the field-free case in order to contain a mode consistent with the observed 626 Hz QPO. The field-free case gives a minimum radius for a crust that can reproduce observations of SGR 1806-20; our model requires $R \geq 11.9\,{\rm km}$ for SGR 1806-20.

The sensitivity of harmonic modes to the magnetic field strength hints at the behavior of the magnetic field with depth. If the value of the magnetic field is constant throughout the crust the surface dipole field must be considered an upper-limit on the field strength in order to find mass and radius solutions consistent with constraints from PREs and LMXBs. The surface dipole field must be a large overestimate of the surface field if the magnetic field were to be larger deeper in the crust. However, the model could allow for a larger surface dipole field than is observed if the magnetic field were weaker deeper in the crust. Alternatively, any configuration of the magnetic field is allowed as long as the field strength is $\lesssim 10^{15}\,{\rm G}$ everywhere in the crust.

The degree of entrainment of the free neutron gas in the inner crust will alter both fundamental and harmonic modes. Crusts with less entrainment require larger masses and radii to have modes consistent with observed QPOs. We must extrapolate outside the EOS curves to approximate a mass and radius for the case of $f_{\rm ent} = 0.50$ which requires a mass of $M = 1.83\,{\rm M}_\odot$ and a radius of $R = 13.9\,{\rm km}$; whereas $f_{\rm ent} = 1.0$ gives $M = 1.35\,{\rm M}_\odot$ and $R = 11.9\,{\rm km}$. The comparison of entrainment fractions can be seen in Figure 4. It was found in Chamel et al. (2012) that entrainment makes global shear modes inconsistent with observed QPOs. In contrast, we find that at least approximately $f_{\rm ent} = 0.75$ is required to have modes consistent with QPOs.

The value of the crust-core transition density can significantly alter harmonic modes. A larger transition density will increase the crust thickness by decreasing $R_{\rm core}$. The thicker crust will have a larger shear velocity on average when integrating a perturbation over the crust. Fundamental modes are only slightly altered by a high transition density. These features can be seen when comparing both panels of Figure 3.

Magnetar giant flare QPOs give us a unique opportunity to probe the neutron star mass-radius relation. Fundamental torsional modes are largely independent of the crust-core transition density and the magnetic field strength. Harmonic modes are sensitive to the details of the neutron star interior: the transition density, entrainment of the free neutrons, and the magnetic field strength. Comparison of fundamental and harmonic modes gives solutions for magnetar masses and radii. Since fundamental and harmonic modes are set by different properties of the neutron star, comparison of these modes gives us insight into the magnetar interior. In particular, we can find the required interior conditions that give solutions for magnetar masses and radii that are consistent with mass and radius constraints from PREs and LMXBs. Solutions most consistent with these constraints have a large degree of free neutron entrainment, large crust-core transition densities, and lower magnetic fields than observed surface dipole fields.

Some of the basic trends observed in the results above have also been observed by Sotani et al. (2013). We also find, in agreement with Sotani et al. (2013), smaller fundamental mode frequencies for crust EOSs with larger values of L, as SLy4 corresponds to $L = 46\,{\rm MeV}$, and Rs corresponds to $L = 86\,{\rm MeV}$. Both works find that more entrainment decreases the fundamental frequency (In the notation of Sotani et al. (2013), $N_s/N_d = 1 - f_{\rm ent}$). Our work includes nuclear shell effects in a more consistent fashion, and thus it is more difficult to vary L continuously as in Sotani et al. (2013). Also, we only employ EOSs that are consistent with recent constraints from neutron star mass and radius measurements (Steiner et al. 2012) that rule out larger values of L. One critical thing missing in both works is a complete evaluation of how the entrainment in the crust might be correlated with L. Work in this direction is in progress.

The authors would like to thank Andrew Cumming and Sanjay Reddy for useful discussions. This work is supported by NASA ATFP grant NNX08AG76G, U.S. DOE grant DE-FG02-00ER41132, Chandra grant TM1-12003X, NSF grant 1109176, and by the Joint Institute for Nuclear Astrophysics at MSU under NSF PHY grant 08-22648.

APPENDIX

THE CRUST EQUATION OF STATE

To compute the energy density of matter in the crust w, we start with an expression similar to that used by Baym et al. (1971a). We take our crust to be composed of "drops" of nuclear matter with volume fraction χ; within the nucleus the density of neutrons and protons are n_n and n_p, respectively, and we denote $n_l = n_n + n_p$ to be the average baryon density inside a nucleus. The dripped neutrons, with density n_{drip}, occupy a fraction $1-\chi$ of the volume. The density of nucleons per unit volume is thus $n = \chi(n_n + n_p) + (1-\chi)n_{\mathrm{drip}}$, and the density of electrons is n_e. As the density approaches nuclear saturation the fraction of space filled by the neutron gas approaches unity.

The energy density w has contributions from nuclei (including the Coulomb lattice contribution), dripped neutrons, and electrons:

$$w(Z,A,n) = \chi\left[n_n m_n + n_p m_p + n_l \frac{E_{\mathrm{bind}}(Z,A)}{A}\right] + (1-\chi)\epsilon(n_n = n_{\mathrm{drip}}, n_p = 0) + w_e(n_e). \tag{A1}$$

This expression is valid for any baryon density below the transition density ($\approx 10^{14}\,\mathrm{g\,cm^{-3}}$). Here $\epsilon(n_n,n_p)$ is the energy density, including rest mass, of homogeneous bulk matter at a given neutron and proton number density. We compute ϵ using the bulk matter Hamiltonian in the Skyrme model (Skyrme 1959) with SLy4 coefficients (Chabanat et al. 1995).

The energy density of the nucleus is

$$n_n m_n + n_p m_p + n_l \frac{E_{\mathrm{bind}}(Z,A)}{A} = \epsilon(n_n,n_p) + \frac{n_l}{A}\left(E_{\mathrm{surf}} + E_{\mathrm{shell}} + E_{\mathrm{pair}}\right) + w_{\mathrm{Coul.}}. \tag{A2}$$

In this expression, n_n and n_p are the neutron and proton densities inside the nucleus. For the nuclear and lattice contributions to the energy density E_{bind}, we use a liquid-drop mass model (Baym et al. 1971a,b; Ravenhall et al. 1983; Steiner 2008) that includes the lattice contribution in the Coulomb term $w_{\mathrm{Coul.}}$, as well as surface (E_{surf}), shell (E_{shell}), and pairing (E_{pair}) corrections to the homogeneous bulk matter Hamiltonian ϵ. At lower densities, the energy per particle in the crust is minimized when $n_{\mathrm{drip}} = 0$, and after the neutron-drip point (about 4×10^{11} g/cm^3), the energy per particle is minimized only when $n_{\mathrm{drip}} > 0$. The baryon number density inside a nucleus n_l is determined from

$$n_l = n_0 + n_1 I^2, \tag{A3}$$

where $I = 1 - 2Z/A$ is the isospin asymmetry, n_0 is the nuclear saturation density of bulk homogeneous matter, and $n_1 < 0$ is a correction due to both the isospin asymmetry, which decreases the saturation density, and the Coulomb interaction, which increases the saturation density (Steiner 2008). The average neutron and proton densities within the nucleus are then determined from n_l and I via

$$n_n = \frac{n_l}{2}(1+\eta I), \quad n_p = \frac{n_l}{2}(1-\eta I), \tag{A4}$$

where $\eta = \delta/I = 0.92$ is a constant of our model that determines the thickness of a neutron skin (Steiner 2008), i.e., the difference between neutron and proton radii, and $\delta = 1 - 2n_p/(n_n+n_p)$ is the density asymmetry.

The next three terms in equation (A2) are the surface, shell, and pairing corrections. The surface correction is proportional to the surface tension σ, the nuclear surface area $A^{2/3}$, and density asymmetry δ,

$$E_{\mathrm{surf}} = \sigma\left(\frac{36\pi A^2}{n_l^2}\right)^{1/3}\left(1 - \sigma_\delta \delta^2\right) \tag{A5}$$

where $\sigma_\delta > 0$ is a parameter that represents the surface asymmetry (Myers & Swiatecki 1969; Steiner et al. 2005). The shell correction to the binding energy per baryon is (Dieperink & van Isacker 2009)

$$E_{\mathrm{shell}}(Z,N) = a_1 S_2 + a_2 S_2^2 + a_3 S_3 + a_{np} S_{np}, \tag{A6}$$

where

$$S_2 = \frac{n_v \bar{n}_v}{D_n} + \frac{z_v \bar{z}_v}{D_z}, \tag{A7}$$

$$S_3 = \frac{n_v \bar{n}_v (n_v - \bar{n}_v)}{D_n} + \frac{z_v \bar{z}_v (z_v - \bar{z}_v)}{D_z}, \tag{A8}$$

$$S_{np} = \frac{n_v \bar{n}_v z_v \bar{z}_v}{D_n D_z}, \tag{A9}$$

and

$$\bar{n}_v \equiv D_n - n_v, \tag{A10}$$

$$\bar{z}_v \equiv D_z - z_v. \tag{A11}$$

TABLE 2
Parameters of the mass model.

parameter	value
n_0	$0.1740\,\mathrm{fm}^{-3}$
n_1	$-0.0157\,\mathrm{fm}^{-3}$
η	0.9208
σ_δ	1.964
σ	1.164 MeV
a_1	-1.217 MeV
a_2	0.0256 MeV
a_3	0.0038 MeV
a_{np}	0.0357 MeV
a_p	5.277 MeV

The parameters D_n and D_z correspond to the degeneracy of the neutron and proton shells, i.e., the difference between the magic numbers enclosing the current amount of neutrons or protons. The quantities n_v and z_v are the number of valence neutrons and protons, i.e., the difference between the current number of protons or neutrons and the preceding magic number. The pairing contribution to the nuclear binding energy is taken from Brehm (1989) with updated coefficients,

$$E_{\mathrm{pair}} = \begin{cases} -a_p A^{-1/2}, & \text{even-even} \\ +a_p A^{-1/2}, & \text{odd-odd} \\ 0, & \text{even-odd} \end{cases}, \tag{A12}$$

where a_p is a constant of our model. The last term in equation (A2) is the Coulomb energy density,

$$w_{\mathrm{Coul.}} = \frac{2\pi}{5} n_p^2 e^2 R_p^2 \left(2 - 3\chi^{1/3} + \chi\right), \tag{A13}$$

where e^2 is the Coulomb coupling and R_p is the proton radius ($3Z = 4\pi n_p R_p^3$). The respective χ terms in parentheses correspond to the Coulomb contribution, the lattice contribution, and a correction that accounts for the filling fraction χ of the nuclei. Table 2 lists the values of the coefficients used in this mass model.

The electronic contribution to the energy density is that of an electron gas embedded in a uniform magnetic field. The electrons acquire an effective mass m_f in the presence of the magnetic field

$$m_f^2 = m_e^2 + 2m_e^2 \left(x + \frac{1}{2} + \frac{1}{2}\nu\right) B_*, \tag{A14}$$

where m_e, x, and ν are respectively the electron mass, principal quantum number, and electron spin along the magnetic field (Rabi 1928; Ventura & Potekhin 2001). Here $B_* = \hbar e B / m_e^2 c^3 = B/(4.414 \times 10^{13}\,\mathrm{G})$ is the ratio of the magnetic field to the critical field, defined as the field at which the cyclotron energy equals the electron rest-mass. The electron number density and energy density are found by summing over electron states and spins in the limit $\mu_e \gg m_f$.

REFERENCES

Barat, C., et al. 1983, A&A, 126, 400
Baym, G., Bethe, H. A., & Pethick, C. J. 1971a, Nucl. Phys. A, 175, 225
Baym, G., Pethick, C., & Sutherland, P. 1971b, ApJ, 170, 299
Brehm, J. J. 1989, Introduction to the Structure of Matter (Wiley)
Broderick, A., Prakash, M., & Lattimer, J. M. 2000, ApJ, 537, 351
Cardall, C. Y., Prakash, M., & Lattimer, J. M. 2001, ApJ, 554, 322
Chabanat, E., Bonche, P., Haensel, P., Meyer, J., & Schaeffer, R. 1995, Phys. Scripta, T56, 231
Chamel, N. 2013, Phys. Rev. Lett., 110, 011101
Chamel, N., Page, D., & Reddy, S. 2012, arXiv:1210.5169
Chamel, N., Pavlov, R., Mihailov, L., Velchev, C., Stoyanov, Z., et al. 2012, Phys. Rev. C, 86, 055804
Dieperink, A. E. L., & van Isacker, P. 2009, Eur. Phys. Jour. A, 42, 269
Duncan, R. C. 1998, ApJ, 498, L45
Farouki, R. T., & Hamaguchi, S. 1993, Phys. Rev. E, 47, 4330
Friedrich, J., & Reinhard, P.-G. 1986, Phys. Rev. C, 33, 335
Glampedakis, K., Samuelsson, L., & Andersson, N. 2006, MNRAS, 371, L74
Harding, A. K., & Lai, D. 2006, Rep. Prog. Phys., 69, 2631
Horowitz, C. J., Schneider, A. S., & Berry, D. K. 2010, Phys. Rev. Lett., 104, 231101
Israel, G. L., et al. 2005, ApJ, 628, L53
Lai, D., & Shapiro, S. L. 1991, ApJ, 383, 745
Lattimer, J. M., & Prakash, M. 2007, Phys. Rep., 442, 109
Levin, Y. 2006, MNRAS, 368, L35
Möller, P., Nix, J. R., Myers, W. D., & Swiatecki, W. J. 1995, At. Data Nucl. Data Tables, 59, 185
Myers, W. D., & Swiatecki, W. J. 1969, Ann. Phys., 55, 395
Nag, N., Ghosh, S., & Chakrabarty, S. 2009, Ann. Phys., 324, 499
Nandi, R., Chatterjee, D., & Bandyopadhyay, D. 2012, arXiv:1207.3247
Newton, W., Gearheart, M., & Li, B.-A. 2013, ApJS, 204, 9
Oyamatsu, K., & Iida, K. 2007, Phys. Rev. C, 75, 015801
Piro, A. L. 2005, ApJ, 634, L153
Rabi, I. I. 1928, Zeitschrift fur Physik, 49, 507
Ravenhall, D. G., Pethick, C. J., & Wilson, J. R. 1983, Phys. Rev. Lett., 50, 2066
Samuelsson, L., & Andersson, N. 2007, MNRAS, 374, 256
Schumaker, B. L., & Thorne, K. S. 1983, MNRAS, 203, 457
Skyrme, T. 1959, Nucl. Phys. A, 9, 615
Sotani, H., Nakazato, K., Iida, K., & Oyamatsu, K. 2013, MNRAS, 428, L21
Steiner, A. W. 2008, Phys. Rev. C, 77, 035805
Steiner, A. W. 2012, Phys. Rev. C, 85, 055804
Steiner, A. W., Lattimer, J. M., & Brown, E. F. 2010, ApJ, 722, 33
Steiner, A. W., Lattimer, J. M., & Brown, E. F. 2012, ApJL, 5

Steiner, A. W., Prakash, M., Lattimer, J. M., & Ellis, P. J. 2005, Phys. Rep., 411, 325
Steiner, A. W., & Watts, A. L. 2009, Phys. Rev. Lett., 103, 181101
Strohmayer, T., van Horn, H. M., Ogata, S., Iyetomi, H., & Ichimaru, S. 1991, ApJ, 375, 679
Strohmayer, T. E., & Watts, A. L. 2005, ApJ, 632, L111
—. 2006, ApJ, 653, 593
van Hoven, M., & Levin, Y. 2012, MNRAS, 420, 3035
Ventura, J., & Potekhin, A. 2001, in The Neutron Star - Black Hole Connection, ed. C. Kouveliotou, J. Ventura, & E. van den Heuvel, 393
Watts, A. L., & Strohmayer, T. E. 2006, ApJ, 637, L117